Cloud and Aerosol Research Capabilities at FARS: The Facility for Atmospheric Remote Sensing

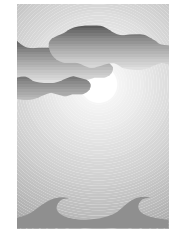

Kenneth Sassen, Jennifer M. Comstock, Zhien Wang, and Gerald G. Mace
Department of Meteorology, University of Utah, Salt Lake City, Utah

ABSTRACT

Since October 1987, the University of Utah Facility for Atmospheric Remote Sensing (FARS) has been applied to the probing of the atmosphere, concentrating on the study of high-level clouds. Regular FARS measurements, which currently total ~3000 h of ruby lidar polarization data, have been directed toward basic cloud research, remote sensing techniques development, and to improving satellite cloud property retrieval methods and GCM predictions by providing climatologically representative cloud datasets and parameterizations. Although the initial studies involved mainly the ruby lidar, the facility has steadily evolved to include a range of visible, infrared, and microwave passive remote sensors, and state-of-the-art, high-resolution dual-wavelength scanning lidar and W-band Doppler radar systems. All three active systems display polarization diversity. In this paper are reviewed the specifications of FARS instrumentation and the research programs to which they have been applied. Four multiple remote sensor case studies of various cloud systems are presented to illustrate the research capabilities. Like a handful of similar sites elsewhere, such research centers dedicated to extended time observation programs have great potential for contributing to atmospheric monitoring and climate research.

1. Introduction

In recent decades the utility of remote sensing instruments for studying the state of the atmosphere has without question been demonstrated. In addition to satellite-borne passive remote sensors, which began as simple gray-level television cameras orbited in the early 1960s, the capabilities of ground-based active remote sensors have also steadily improved. Currently, a variety of lidar optical and radar microwave measurement technologies are available for atmospheric research. Particularly promising for aerosol and cloud research are polarization lidar and millimeter-wave radar, which are both planned for deployment soon on orbiting platforms for the purpose of climate-oriented global research.

The research capabilities of modern remote sensors have been illustrated in several recent field research campaigns, such as those designed to study cirrus and stratus clouds in the First International Satellite Cloud Climatology Program (ISCCP) Regional Experiment (FIRE; Cox et al. 1987). The climatic impact of both types of clouds is not rigorously understood, even though their role in maintaining the global radiative balance is likely to be significant. In such experiments, groups of mobile passive and active remote sensors and supporting aircraft have been assembled to generate highly synergistic datasets.

On the other hand, in view of the advantages in some respects of extended time atmospheric *monitoring*, many permanent field sites now exist that support one or more remote sensing instruments, such as the global and regional networks of aerosol lidars. Only a few facilities, however, can fully take advantage of the principal of remote sensor synergy by deploying the types of diverse instruments gathered together at major field experiments. As first demonstrated using complementary multiple remote sensors in winter mountain storms (Sassen 1984), in which each sensor was shown to have both unique capabilities and limitations, combined passive–active, visible–infrared–microwave remote sensing leads to the best characterization of the cloudy atmosphere. This fact is at the foundation of

Corresponding author address: Kenneth Sassen, 135 S 1460 E (819 WBB), University of Utah, Salt Lake City, UT 84112.
E-mail: ksassen@met.utah.edu
In final form 9 January 2001.
©2001 American Meteorological Society

the design of the Clouds and Radiation Testbed (CART) sites supporting the Department of Energy's Atmospheric Radiation Measurement (ARM) program (Stokes and Schwartz 1994) and the University of Utah Department of Meteorology Red Butte field site described here.

2. The Facility for Atmospheric Remote Sensing

A meteorological field station was established in 1978 at the mouth of Red Butte Canyon on the eastern edge of the University of Utah campus to house the mobile cloud polarization lidar (CPL) (and its predecessor), which participated in several aerosol and cloud research programs, and an M-33 radar (Sassen 1980). The site is located at 40° 49′00"N and 111° 49′38"W at the base of the Wasatch Mountains at 1.52-km MSL (all heights are given above mean sea level), overlooking the Salt Lake Valley and southern Great Salt Lake. It lies ~12 km west of the Salt Lake City (SLC) National Weather Service (NWS) station, which provides upper air sounding profiles twice daily.

A permanent research station designed to house the CPL and accommodate additional instrumentation, the Facility for Atmospheric Remote Sensing (FARS) was constructed in 1987 with joint funding from the National Science Foundation and the University of Utah. This facility was equipped with a rooftop parapet for mounting radiometers, a porch for radar studies, and a paved area for mobile instrument vans, which were to be gradually added. As described below, these additions include a suite of visible, infrared, and microwave radiometers; photographic and video all-sky imagery; and state-of-the-art 3.2-mm Doppler radar and dual-wavelength scanning polarization diversity lidar (PDL) systems. The radar and PDL are mobile units that have participated in several aircraft-supported cloud research programs at the Southern Great Plains (SGP) ARM CART site. Each system has a computer controller–data acquisition unit, which is linked to the main campus via the internet. The specifications of these instruments are provided in Table 1.

A common feature of the three active remote sensing systems is polarization diversity (Sassen 2000). As is reflected in the instrument designs, our data collection philosophy has stressed examining the extra information content inherent in measuring the change in the state of polarization of the backscattered energy. This research tool becomes even more useful in view of the principle of exploiting basic particle scattering differences over the large 0.532-μm to 3.2-mm range of wavelengths, where hydrometeor scattering spans the geometric optics and Rayleigh domains. In all three devices, linear depolarization ratios, or δ values, are derived from the backscatter when transmitting linearly polarized pulses (see Table 1 for pulse planes). The δ value is the ratio of the energy returned in the perpendicular-to-parallel polarization planes, after corrections are made for differences in the receiver channel gains.

a. Instrumentation

1) The cloud polarization lidar

As can be seen from the photograph of the interior of FARS in Fig. 1, the CPL is mounted on a (manually) scannable table and yoke located beneath a skylight, and, with component replacements, has been continually in use since 1987. Some components of this "turnkey" lidar can be traced back to one of the earliest systems developed in the mid-1960s at New York University (Schotland et al. 1971). The design of the dual-polarization receiver is based on the use of a variable field stop diaphragm, laser line interference filter, Glan-air polarizing prism, and two photomultiplier tubes (PMTs) to simultaneously measure the energy returned from the vertically polarized laser in the horizontal and vertical planes (Sassen 2000). The δ value is computed after adjusting for differences in electronic gains and optical misalignment. Calibrations are performed with the use of a randomly polarized

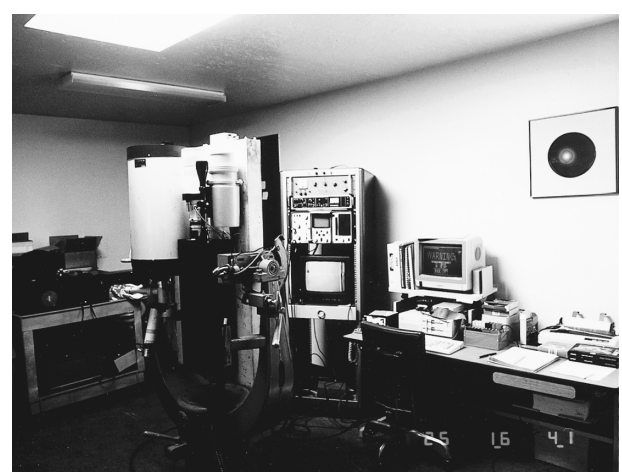

Fig. 1. Interior view of FARS showing the zenith-pointing cloud polarization lidar and coaligned midinfrared radiometer beneath the observation skylight, along with some of the computer controllers and video systems.

TABLE 1. University of Utah Facility for Atmospheric Remote Sensing (FARS) instrumentation.

1) Passive remote sensors
   (a) Net flux pyradiometers
   (b) Narrow-beam (0.14°) 9.5–12.5-μm radiometer (coaligned with lidar)
   (c) Precision infrared radiometer
   (d) Pyradiometer, 0.3–2.8-μm broadband visible
   (e) Multiple frequency RSR (6 channels, 0.415–0.94-μm, 10-nm bandpass)
   (f) Pyrheliometer (0.63–2.8 μm) with solar tracker
   (g) Sun photometer (10 channels, 0.38–1.03-μm, 10-nm bandpass)
   (h) Dual-channel (31.4 and 23.8 GHz) microwave radiometer
   (i) All-sky 35-mm photography
   (j) All-sky video time-lapse imagery
2) Active remote sensors
   (a) Cloud polarization lidar (CPL) two channels
      - vertical polarization transmitted
      - manually "tiltable" ±5° from zenith
      - 0.1-Hz PRF, 7.5-m max range resolution
      - max 2 K per channel data record length
      - 1–3-mrad receiver beamwidths
      - 25-cm diameter telescope–
      - 0.694-μm wavelength, 1.5 maximum output
   (b) Polarization diversity lidar (PDL)
      - Four channels
      - Vertical (0.532 μm) and horizontal (1.06 μm) polarizations
      - Fully scannable, 5° s^{-1}
      - 10-Hz PRF, 1.5-m maximum range resolution
      - 2–8 K per channel data record length
      - 0.2–3.8-mrad variable receiver beamwidths
      - 35-cm diameter telescope (two)
      - Simultaneous 0.532- and 1.06-μm wavelengths, 0.45-J outputs
   (c) 95-GHz polarimetric Doppler radar
      - Six channels (two Doppler)
      - Vertical and horizontal polarizations transmitted
      - Fully scannable, 5° s^{-1}
      - 10 Hz–80 KHz PRF, 7.5-m max range resolution
      - 600 range gates
      - 0.25° beamwidth
      - 90-cm diameter dish, 57-dB gain
      - 3.2-mm wavelength, 1.2-KW peak power

light source positioned at the minimum telescope focus distance.

Note from Table 1 that this relatively high-power ruby lidar system has a low pulse repetition frequency (PRF) and is normally digitized with a maximum record length of 2048 8-bit samples at a range resolution of 7.5 m (i.e., 16.17-km MSL maximum altitude). In other words, it generates a manageable amount of data, which facilitates the development of an extended remote sensing dataset. On the other hand, the sensitivity of the unit is sufficient to treat each pulse as independent (i.e., no averaging is required for most tropospheric targets). Over the years a steady improvement in CPL data acquisition has been made by upgrading (from the original Apple IIe) to faster PCs, but a common format for data archival has been used

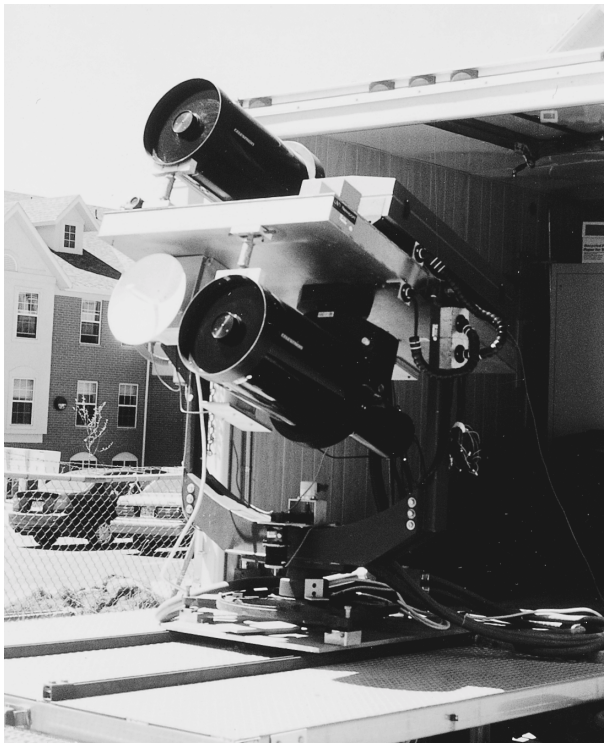

FIG. 2. Photograph of the polarization diversity lidar deployed at FARS for scanning operations on the mobile platforms rear tailgate, depicting the laser transmitter, dual telescope receivers, and safety radar unit dish.

throughout. A two-channel digital oscilloscope, with a pretrigger capability to obtain background light levels, has served as the returned signal digitizer for this low-PRF lidar.

Also visible at upper right on the lidar table in Fig. 1 is a coaligned narrow beam midinfrared radiometer (see Table 1) for combined lidar–radiometer (LIRAD) cloud studies (Platt et al. 1987; Barnett 2000). Not visible in this photograph, but important for safety purposes and to facilitate the preparation of field notes, is a video camera also coaligned with the lidar.

2) THE POLARIZATION DIVERSITY LIDAR

Based on a commercial Nd:YAG laser, the PDL was designed to be a testbed of lidar polarization techniques for cloud and aerosol research (Sassen 1994). Permanently truck mounted, this unit replaced the mobile CPL for field research, making its first appearance in the 1991 FIRE second Intensive Field Observing campaign in Coffeyville, Kansas. The lidar table can be either pointed out a roof hatch for zenith measurements and ±10° zenith scans, or positioned on a rear tailgate for range–height indicator scans (see Fig. 2). This 10-Hz PRF lidar has simultaneous four-channel, two-color (0.532 and 1.06 μm) linear polarization capabilities at range resolutions down to 1.5 m, making it a uniquely high resolution scanning lidar. Each wavelength has its own steerable telescope receiver using the same dual-channel design as the CPL, except light detection at 1.06 μm uses a pair of silicon avalanche photodiodes instead of PMTs. The receivers are also equipped with computer-controlled diaphragms for variable field-of-view (FOV) multiple scattering studies.

Because of scanning laser eye safety concerns, also mounted on the PDL table is a modified X-band marine radar unit (Fig. 2), which with a PC controller serves as a laser interrupt device if aircraft encroach within ~2.5° of the lidar FOV. It has been fully tested during CART research involving various aircraft, including the high-flying National Aeronautics and Space Administration (NASA) ER-2.

3) THE W-BAND POLARIMETRIC DOPPLER RADAR

The National Science Foundation Academic Infrastructure Program and the University of Utah provided funding for a research grade 95-GHz (3.2 mm) radar to join the FARS instrumentation suite in order to evaluate the cloud research potential of such emerging millimeter-wave technologies. The radar was manufactured in 1994 by Quadrant Engineering, Inc., of Amherst, Massachusetts and has been applied to basic cloud research and teaching at FARS and during SGP CART campaigns (Sassen and Chen 1995). Figure 3 shows the radar on a scanning pedestal positioned on the FARS porch during recent instruction of a Radar Meteorology class.

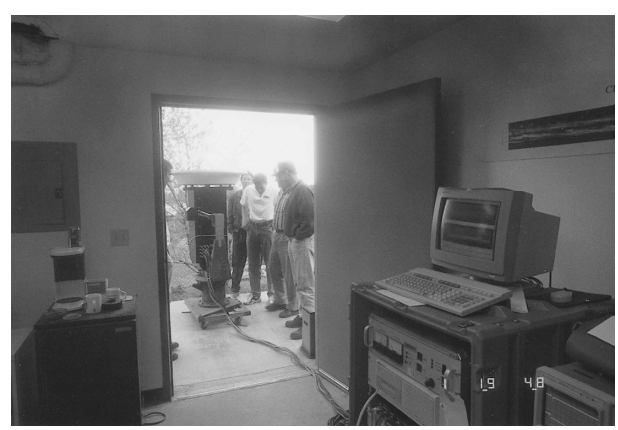

FIG. 3. The 95-GHz Doppler radar deployed on the FARS porch during the instruction of a Radar Meteorology class. Computer and transmitter component rack is partially seen at right.

This scannable radar is powered by a 1.5-kW Klystron transmitter, with the 0.9-m diameter dish allowing for a 0.25° beamwidth (Table 1). The radar provides six data channels, including horizontally plus vertically polarized co- and cross-polar radar reflectivity factors, and Doppler radial velocities. Recent computer hardware and software upgrades allow the collection of full Doppler spectra instead of the standard pulse-pair estimated values.

Radar calibrations have previously been obtained through comparison with radar reflectivities derived from stratus cloud in situ data, and through intercomparisons with other cloud radars at the SGP CART site. We now have the ability to perform absolute calibrations through the use of a corner reflector mounted near FARS. Relative radar calibration is tracked using an internal signal loop that monitors changes in the transmitting and receiving subsystems.

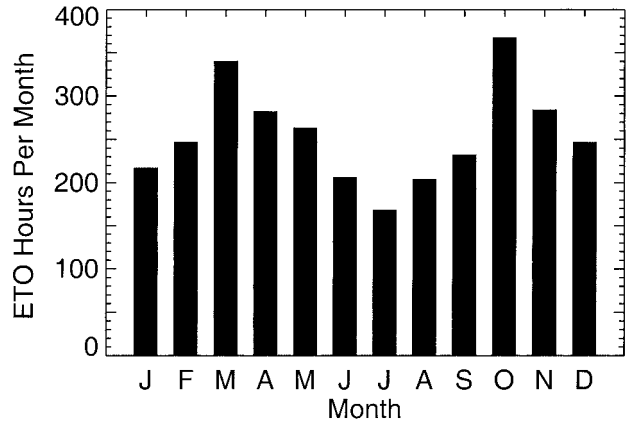

FIG. 4. Bar graph depicting the monthly totals of FARS CPL cloud and aerosol data collected from Oct 1987 to Dec 2000. Concentrating on cirrus cloud research, the monthly distribution of measurements agrees well with the local NWS reports of high cloud amounts (Sassen and Campbell 2001).

4) PASSIVE REMOTE SENSORS

As shown in Table 1, a variety of hemispherical, solar tracking, direct and diffuse, and zenith radiometers operate in the visible, infrared, and microwave spectral regions. Cloud and aerosol visible optical depth τ can be retrieved using several of these devices, downwelling cloud layer infrared emittance ε with the narrowbeam midinfrared radiometer, and precipitable water vapor and liquid water depths with the dual-channel microwave radiometer (MWR). These range-integrated data quantities are important adjuncts to the analysis of the active remote sensing data. All-sky color and red-filtered, black-and-white, 35-mm fisheye photographs are regularly collected, as well as occasional all-sky and zenith time lapse video imagery.

b. FARS research objectives

Since FARS was established in 1987, it has been applied to the regular study of high-level clouds in support of basic cirrus research, and the polar-orbiting and Geostationary Operational Environmental Satellite (GOES) cloud property validation effort of the Project FIRE Extended Time Observation (ETO) component. Additional foci that have contributed to the scope of our research have included an emphasis on thin/subvisual cirrus studies from 1988 to 1989, two Experimental Cloud Lidar Pilot Study program cloud study periods (Platt et al. 1994), enhanced contrail research from 1993 to 1996, and since 1998 an aircraft-supported Earth Observing System (EOS) Terra satellite cloud property validation program. Figure 4 shows the monthly totals of ETO measurement hours since the inception of FARS, which, although concentrating on cirrus cloud observations, also contains many intentional and unintentional opportunities for studying aerosols and other cloud types (Campbell 1997). As of December 2000, more than 3000 h of ruby lidar data and nearly 12 000 two-color fisheye photographs have been collected, largely in accordance with the ephemeris of National Oceanic and Atmospheric Administration (NOAA) polar-orbiting satellite overpasses. Most measurements have involved the afternoon and evening hours corresponding to local polar orbiter imagery. We typically attempt to obtain ~3 h observation periods in order to encompass multiple satellite overpass opportunities, and to obtain records corresponding to the passage of mesoscale features of advecting cirrus cloud systems.

As a result of the ETO activities based firmly on the visual identification of cloud type (Sassen 2001a), we have been able to develop climatologically representative characterizations of the essential properties of the midlatitude cirrus clouds inhabiting the eastern Great Basin of the United States. Studies of frequent aircraft condensation trails (contrails) in our area are described in Sassen (1997). The mean and monthly variabilities in macrophysical cirrus cloud properties, and an analysis of their associated synoptic weather patterns, are given in Sassen and Campbell (2001). In Sassen and Benson (2001) are described cloud microphysical properties inferred from lidar depolarization, including the basic temperature dependence in cirrus particle shape and orientation. Finally, the fundamen-

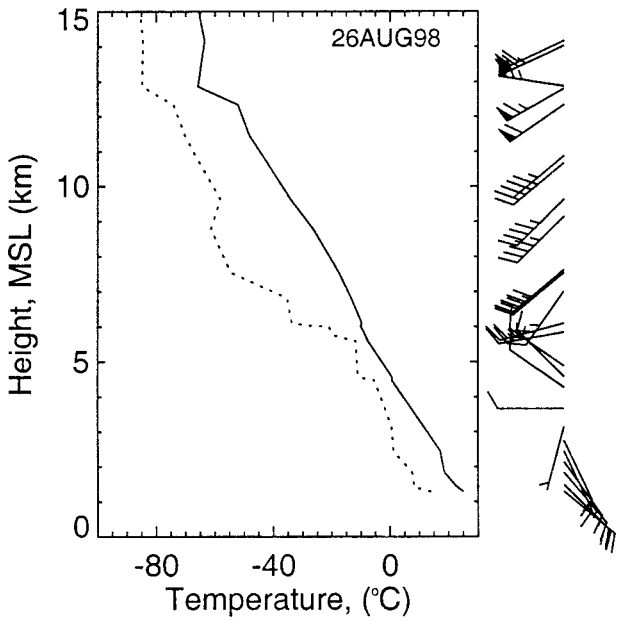

FIG. 5. SLC NWS sounding for 0000 UTC 26 Aug 1998, showing southwesterly monsoonal flow conditions associated with summertime thunderstorm activity. Wind barbs in this and following soundings are given in 2.5, 5.1, and 25.6 m s^{-1} intervals.

tal radiative properties of τ and ε for cirrus generated by various mechanisms (i.e., synoptic, deep convective, and orographic) are characterized in Sassen and Comstock (2001) using the LIRAD method. Additional parameterizations of these quantities in terms of midcloud temperatures and physical cloud thicknesses of high and midlevel clouds are offered in Sassen et al. (2001).

In addition to these climatological findings, there have been numerous opportunities to describe case study and limited climatological results. These have included the properties of corona-producing cirrus clouds (Sassen 1991), thin/subvisual cirrus (Sassen and Cho 1992), contrails (Khvorostyanov and Sassen 1998), and volcanic (Sassen and Horel 1990; Sassen et al. 1994) and free-tropospheric (Sassen 2000, 2001b) aerosols.

While our research has emphasized cirrus clouds (with visible optical depths < ~3.0), we have also taken advantage of the capabilities of the millimeter-wave radar and MWR to perform case studies of other clouds. Whereas high, cold cirrus clouds are most completely observed using lidar, combined microwave and light measurements become a necessity in midlevel, mixed phase, and precipitating cloud systems. In such clouds optical attenuation can become a severe range-limiting factor for lidar. As we will illustrate here for clouds ranging from cirrus to precipitating nimbostratus, the combined use of visible, infrared, and microwave sensing techniques yields a unique synergy in revealing the nature of clouds. As far as aerosol research is concerned, opportunities to use lidar and solar radiometric observations have emerged to study the evolution of volcanic stratospheric aerosols following the June 1991 Mount Pinatubo eruptions, smoke layers from local and regional forest fires, local pollution as part of the October 2000 Vertical Transport and Mixing Experiment, and the remnants of dust storms from as far away as the Mongolian Desert (Sassen 2001b).

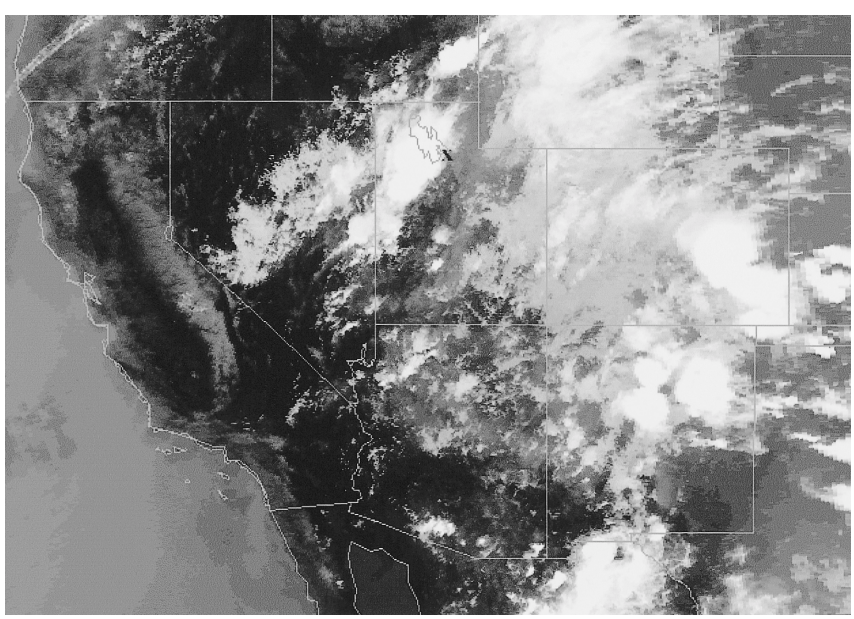

FIG. 6. *NOAA-12* polar-obiter infrared image of the western United States from 0107 on 26 Aug 1998 of the thunderstorms developing just to the southwest of FARS (x symbol).

3. FARS case studies

To demonstrate the capabilities of this remote sensing ensemble for researching tropospheric clouds and aerosols, we provide four FARS case studies comprising various atmospheric conditions. In each case we utilize data from those remote sen-

sors that contribute most to comprehending the specific atmospheric conditions.

a. Cumulonimbus cloud

As shown in the 0000 UTC (all times are universal time coordinate) SLC NWS sounding in Fig. 5, the thunderstorm studied on 26 August 1998 by the CPL and PDL units was associated with southwesterly monsoonal flow. The polar-orbiter satellite image in Fig. 6 depicts this cumulonimbus as it developed in an area enclosed by a severe thunderstorm warning box over the West Desert of Utah, and advected over FARS. The two fisheye photographs at the top of Fig. 7 depict the anvil approaching from the southwest at

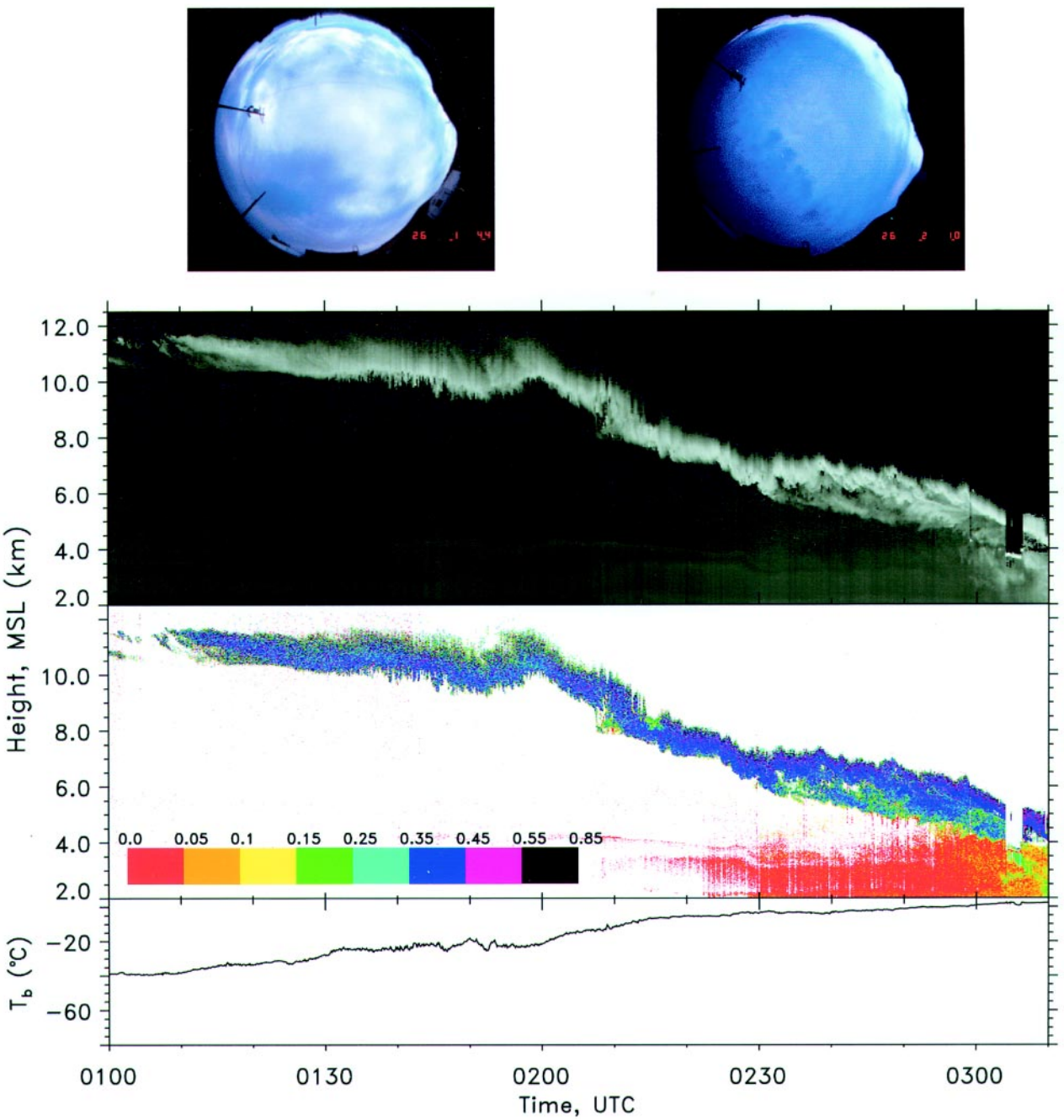

FIG. 7. Time–height displays of CPL relative returned (i.e., not attenuation corrected) energy (top, based on a logarithmic gray scale), and δ-values (see color key) from a thunderstorm as it advected over FARS, bringing rain by 0310 on 26 Aug 1998. At top are two fisheye photographs of all-sky cloud conditions obtained at the times stamped, and at bottom the record of the midinfrared column brightness temperature T_b.

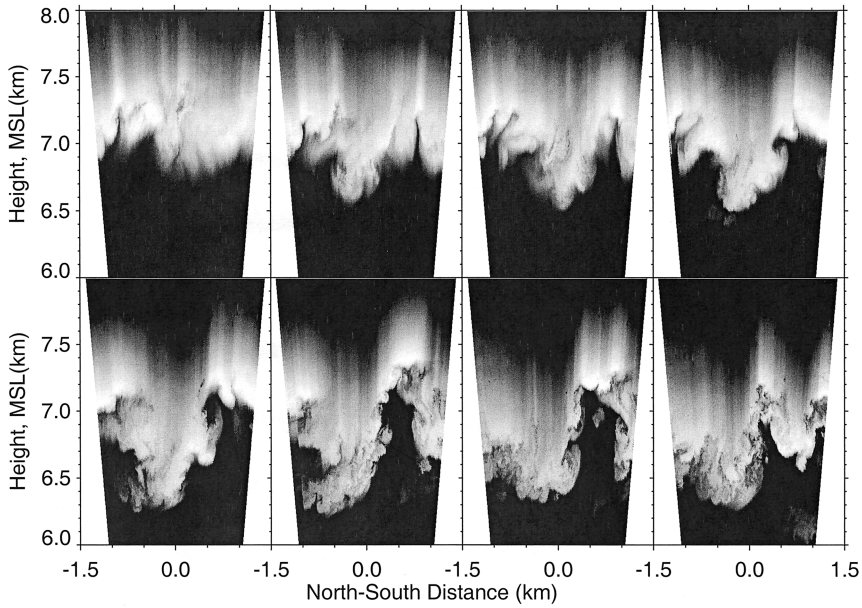

FIG. 8. Consecutive ±10 zenith elevation angle scans of returned energy collected by the PDL from 0225:36 to 0228:38 on 26 Aug 1998 at a 1.0° s^{-1} scan rate, showing high-resolution slices through anvil mammatta.

0144 (note the still-clear skies to the north, at top), and the darkening anvil and large mammatta (center) at 0210. The CPL displays of relative returned energy(in arbitrary units based on a logarithmic gray scale) and laser linear depolarization (see color key) below capture the developing cloud for a ~3 h period, from the initial thin anvil cirrus to the start of rainfall. These displays reveal the typical progression in lidar cloud returns under such increasingly attenuating conditions. It is probable that the anvil cloud top remained at ~12 km, even though the strong optical attenuation produced by the thickening anvil after ~0200 usually limited the range of lidar probing to ~1.0 km. Note the corresponding increase in infrared column brightness temperature T_b over this period (bottom panel). Anvil mammatta first appeared at ~0135, where they can be seen in Fig. 7 to penetrate several hundred meters into the subcloud air.

The lidar depolarization data first indicate rainfall beginning at ~0300. In contrast to the $\delta \approx 0.4$ through most of the ice cloud, the δ in the rain vary from < 0.05 to ~0.2 in response to raindrop-shape oscillations in rain shafts containing differently sized particles, and perhaps to melting graupel or hailstones. The liquid cloud layer that appeared briefly from 0304 to 0307 at 3.7 km is identified by both the very strong optical attenuation it produces and the near-zero δ at cloud base, followed by a rapid increase due to multiple scattering induced depolarization. Just after this time, a lidar *dark band* is visible at 3.9 km where the depolarization decreases rapidly (see also the fourth case study), somewhat below the 4.5-km freezing level (Fig. 5). This feature was first described in Sassen and Chen (1995), and was attributed to the decrease in lidar backscattering caused by the inhomogeneous particles formed just after severely melted snowflakes collapse into raindrops. Finally, note that the aerosol in the boundary layer, which increases as the thunderstorm outflow winds affect the area, produce $\delta < 0.05$, indicative of spherical or (more likely) relatively small nonspherical particles.

Although W-band radar data, which would have been useful in quantifying the range-limited optical conditions, are unavailable, the PDL was utilized after 0200 to collect (0.532 μm) parallel-polarized ±10° elevation angle scans from the zenith direction. These north–south scans represent cross sections approximately orthogonal to the mean cloud-level wind direction (Fig. 5), such that the cloud structural variability across the prevailing winds can be assessed. The high- (1.5-m range by 0.1-s time) resolution example provided in Fig. 8 shows eight consecutive slices through anvil mammatta advecting through the scanning plane (see Fig. 7 fisheye at upper right). At this unique resolution, mammatta are revealed as optically dense, downward-penetrating cloud masses that shed eddies of various scales during mixing with the dry subcloud air.

b. Aircraft condensation trails and elevated aerosols

On 5 March 1999 the passage of a mesoscale cirrus cloud band with contrails particularly evident

FIG. 9. FARS dataset for the 5 Mar 1999 case study of triple lidar wavelength depolarization from cirrus, contrails, and an Asian dust layer. Shown from top to bottom are representative fisheye photographs, CPL returned energy and δ time–height displays, traces of the broadband visible PSP and infrared PIR hemispherical fluxes, T_b, and expanded PDL displays of contrails from near the end of the period.

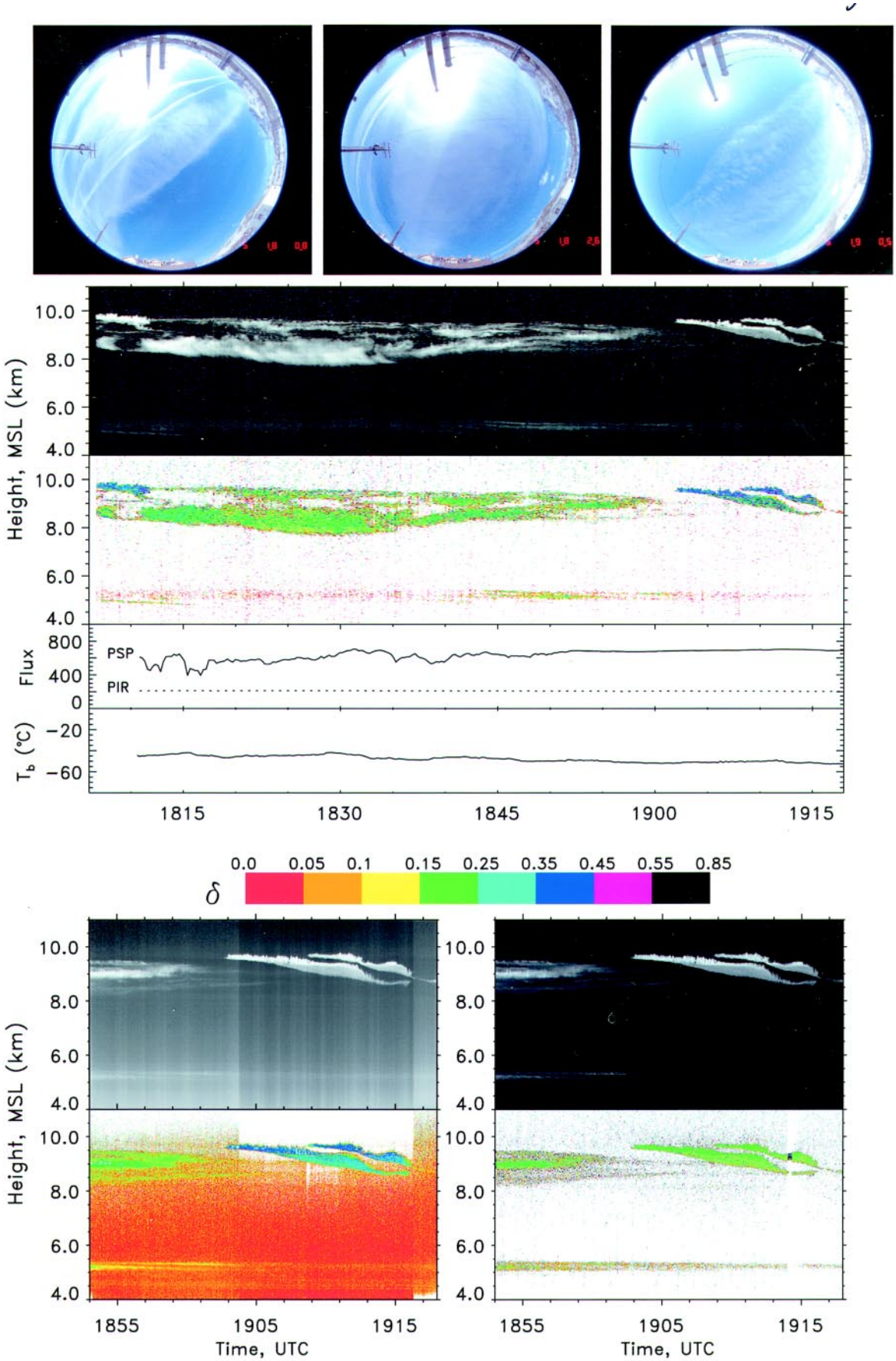
Height, MSL (km)
10.0
8.0
6.0
4.0
Flux
800
400
0
PSP
PIR
T_b (°C)
−20
−60
1815
1830
1845
1900
1915
0.0
0.05
0.1
0.15
0.25
0.35
0.45
0.55
0.85
δ
1855
1905
1915
Time, UTC

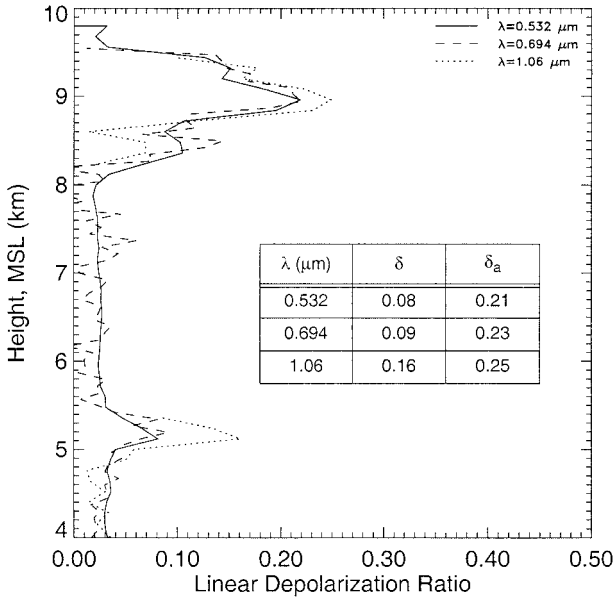

λ (μm)	δ	δ_a
0.532	0.08	0.21
0.694	0.09	0.23
1.06	0.16	0.25

FIG. 10. Comparison of 5-min averaged (1854–1859) δ-value profiles for the three lidar wavelengths during a period when the backscattering from the elevated aerosol layer was relatively strong. The inserted table gives the δ values at the 5.25-km aerosol peak in terms of combined molecular and aerosol δ and estimated aerosol-only δ_a values. Note that the pulse averages varied from 30 to 3000 shots for the CPL and PDL, respectively.

along its leading and trailing edges was studied with backscatter depolarization at the three CPL and PDL wavelengths. Figure 9 compiles the basic active and passive remote sensing data for this lidar case study. Although the W-band radar was not activated, experience has shown that persisting contrails (and very thin cirrus) generally have reflectivities below the detection threshold of millimeter-wave radars because of the relatively small ice particle sizes in contrails (see Sassen and Khvorostyanov 1998).

At the top of Fig. 9 are shown representative fisheye photographs of the persisting linear contrails and thin cirrus cloud, which produced a colorful 22° halo. It can be seen from these images and the CPL displays that the contrails occurred just above the cirrus cloud top at the beginning (missing the contrails leading edge) and at the end of the period, when two contrails passed overhead in succession. The contrails can be identified in the lidar display by the narrow, but strongly backscattering, convective-appearing layers lying above crystal fallstreaks (Sassen 1997). These contrails were estimated to be on the order of 1 h old when sampled in the zenith. Analysis of the radiative effects of the contrails is complicated by the effects of the background cirrus layer, but their impact does not appear to be significant in the infrared spectral region [note the precision infrared radiometer (PIR) and T_p traces] in agreement with an earlier FARS case study (Khvorostyanov and Sassen 1998). This finding implies the presence of relatively small ice particles.

More light is shed on this issue by the 0.532- and 1.06-μm PDL displays at the bottom of Fig. 9. Although the returned energy displays of the two trailing contrails at the two wavelengths are similar, the δ values are not. The significantly lower contrail δ values at the longer wavelength at right implies the presence of small (i.e., relative to the incident wavelength) nonspherical particles, as assessed in Mishchenko and Sassen (1998). Note that the δ values in the thin cirrus are, as is typically the case, quite similar. (Some discrepancies, however, can be expected due to differences in detector noise, frequency response, digitizer gain setting, and scattering volumes sampled.) Using a typical T-matrix scattering theory prediction for nonspherical particles form Mishchenko and Sassen (1998), we can estimate from the depolarization differences that the effective ice particle sizes in the contrails are ~2.0 μm diameter, despite the fact that the contrails were about 1 h old.

Since only small differences in depolarization are found in the cirrus layer at the three lidar wavelengths, it can be concluded that contrails are unique, for clouds that is, in their ability to generate and maintain the sufficiently minute ice particles to manifest a scatter-

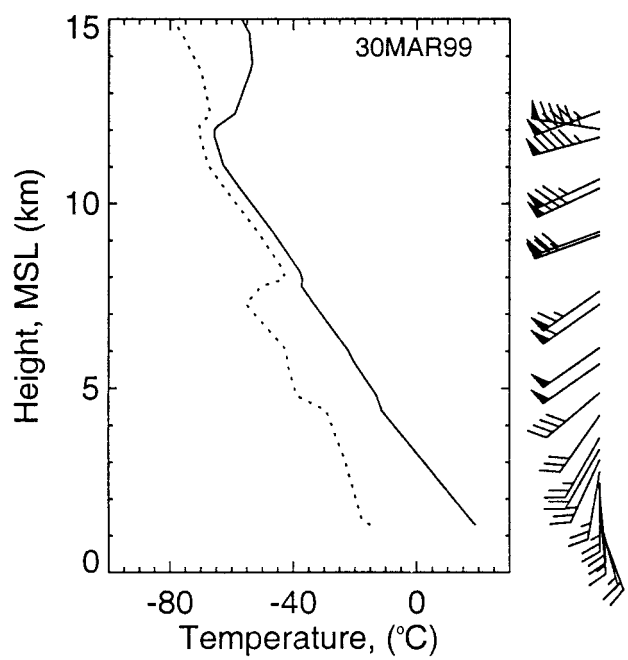

FIG. 11. SLC NWS sounding for 0000 UTC 30 Mar 1999.

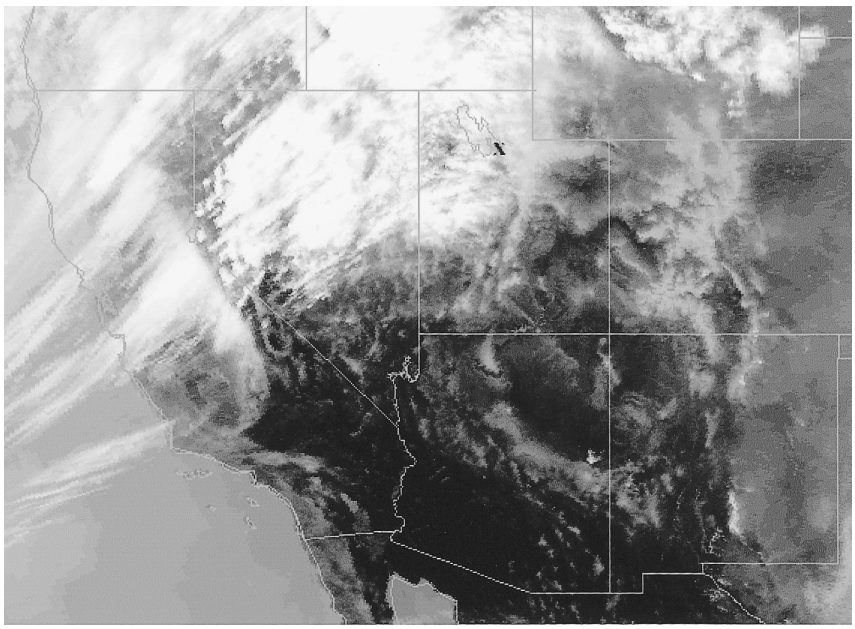

FIG. 12. Infrared channel image obtained during the *NOAA-14* satellite overpass of FARS (x symbol) at 2210 on 29 Mar 1999.

ing dependence in the Rayleigh–Mie transition zone. An additional subject of interest in this regard is the depolarizing behavior of the elevated aerosol layer centered at ~5.3 km in Fig. 9. This aerosol was a product of the transpacific transport of dust from Asian dust storms (Husar et al. 2001), which is not infrequently observed over FARS in the spring. As more clearly shown in the 5-min average profiles in Fig. 10, the δ values at the three wavelengths reveal differences that are related to the impact of the combined molecular (i.e., wavelength to the fourth-power dependent) and nonspherical dust particle backscattering, with maximum δ ranging from 0.08 to 0.16. The inserted table shows the corresponding aerosol-only peak δ_a when the molecular contributions are approximately removed using a range-squared signal filter. In this case, δ_a are ~0.20, which are similar to the Kosa dust-dominated δ values measured in Japan from supermicron-sized particles (Sassen 2000).

c. Cirrostratus-to-altostratus cloud transition

On 29 March 1999 a synoptic-scale arc of high- and middle-level clouds preceding a maritime Pacific storm system swept over northern Utah. Given in Fig. 11 is the 30 March Salt Lake City (SLC) radiosonde data, and in Fig. 12 the *NOAA-14* infrared image of the cirrus over the western United States obtained at 2210. The irradiance records in Fig. 13 provided by the Multiple Frequency Rotating Shadowband Radiometer (MFRSR) are illustrative of the cloud conditions over the daylight period. The passage of an initial band of cirrus from ~1600 to 1930 is revealed by the decrease in direct normal and increase in diffuse horizontal solar irradiances. Following a relatively cloud-free period, a gradually thickening cirrus layer caused a strong reduction in the direct normal solar radiation until by ~2300 the cloud effectively blocked the direct beam.

CPL observations began at 1803 as the initial band of thin cirrus exited the region, and just in advance of the gradually deepening cirrostratus. The fisheye photographs at the top of Fig. 14 follow this cloud evolution, which is further described by the CPL height versus time plots of relative returned energy and depolarization given just below. After the initial cirrus at ~9 km departed, the next cirrus layer with cloud tops to near the 12-km tropopause (Fig. 11) gradually thickened and eventually produced optical attenuation strong enough to cause range-limiting effects at ~2230 and again at 2300. By this time, the

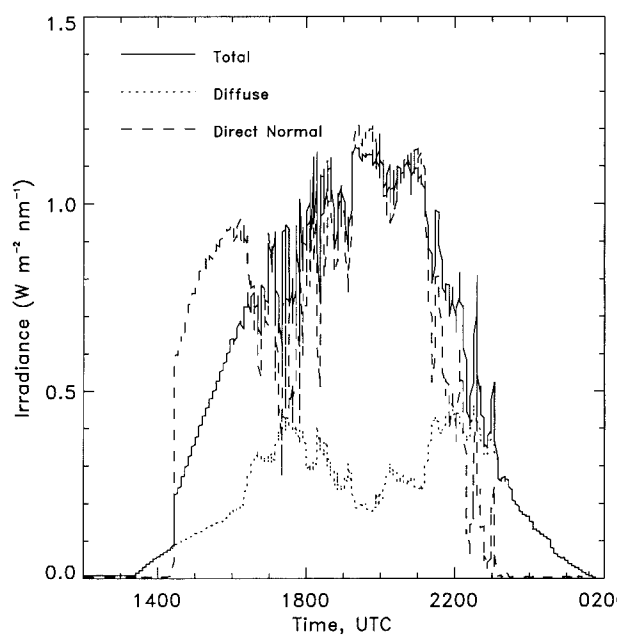

FIG. 13. Solar irradiances displays in the indicated 0.673-μm channels of the MFRSR on 29 Mar 1999.

cloud layer had thickened sufficiently to be classified as altostratus (i.e., the solar disk had become visually indistinct, as shown in the final fisheye photograph).

The laser depolarization display in this cirrus, which generated various optical displays, is particularly interesting. The initial decaying cirrus layer contains low $\delta \approx 0.2$ values, perhaps indicating the rounded crystal forms associated with particle evaporation effects. The strongly scattering and nondepolarizing cloud element sampled briefly at ~1955 at ~9 km, however, represents a persistent contrail composed of horizontally oriented plate crystals (see lower part of the 2005 UTC fisheye). (This was confirmed by scanning the lidar a few degrees off the zenith direction to identify the backscattering anisotropy.) The highest ($\delta \approx 0.55$) depolarization in the higher cirrus layer occurs at the top of the initial mesoscale generating cloud mass (see also the bottom-left display in Fig. 15). At 2005 a three-ringed solar corona was noted in connection with this cloud feature. On the other hand, considerably lower δ values are found between ~2130 and 2230, when a 22° halo was often observed (see the 2122 UTC fisheye). That the special shapes and orientations of the ice crystals generating coronas and halos is reflected in different lidar δ values has been firmly established by recent FARS research (Benson 1999). Finally, strong depolarization at the bottom of the altostratus is observed, likely indicating the presence of ice crystal aggregates. The nature of the weakly scattering, low-depolarizing subcloud layer at 8 km is discussed below.

A comparison between the broadband visible precision solar pyradiometer (PSP), and infrared PIR hemispherical flux and T_b traces in Fig. 14, shows the typical inverse relation between the solar and terrestrial fluxes. That is, increases in cirrus cloud visible optical depth reduce the solar transmittance, but at the same time increase the infrared emittance. This is especially apparent in the PSP versus PRT-5 records, but can also be seen to a lesser extent in the broadbrand PIR data, which is dominated by gaseous emissions under these conditions. The MWR reveals small water vapor depth variations in phase with the presence of the cirrus (note the minimum at ~1900). Finally, the τ and ε derived using 2-min ruby lidar and midinfrared radiometer data averages with the LIRAD method follow the variations in cirrus radiative properties (Barnett 2000). Note the typical graybody ($\varepsilon < 1.0$) nature of the cirrus, and how the light extinction and infrared emission properties vary in phase with one another. By the end of the period, τ approaches 3.0 and ε approaches 1.0, characteristics of the cirrostratus-to-altostratus cloud transition (Sassen 2001a; Sassen et al. 2001).

Additional components of this case study include the PDL and radar height–time displays in Fig. 15 during the thickening of the cirrostratus into altostratus. Shown are the PDL returned energy, and W-band equivalent radar reflectivity factor (Z_e, with lidar-derived cloud boundaries indicated by the dot symbols) and mean Doppler velocities V. It is clear that quite different images of the cloud are generated in the optical (0.532 μm) and microwave (3.2 mm) regions. Although the lidar generally detects the cirrus cloud top at 11.8 km, the radar is insensitive to the smallest ice crystals generated in the upper cloud region. Instead, the radar has detected only those cloud portions, generally associated with generating regions and crystal fallstreaks, containing relatively large and/or numerous particles. As a matter of fact, the strongest Z_e correspond to the "holes" in the lidar returns produced by strong optical attenuation. The mean Doppler velocities provide additional information. The dense cloud mass at ~2230 is revealed to contain a series of alternating up- (as high as 0.5 m s^{-1}) and downdrafts indicating active growth from cloud base. The next pulse of altostratus cloud displays some cellularity, but is often dominated by strong downward motions in excess of 1.0 m s^{-1}, indicating the fallspeeds of ice particle aggregates in this optically dense cloud.

Finally, depicted in the bottom of Fig. 15 are higher-resolution PDL returned power displays of details of the cloud structure. (Note that the δ values at the PDL wavelengths are again very similar to the ruby values, although some differences due to contributions from molecular scattering and noise effects are evident.) The first display (left) shows the initial corona-producing mesoscale cirrus generating/fallstreak structure, where cloud-topped generating cells have produced a ~2 km deep cirrus mass: a relatively strongly scattering thin cloud layer (perhaps of orographic origin) is also present at 9.7 km.

The second detail of the lower cloud region corresponds to a period of strong penetrative fallstreaks, or cirrus mammatta (see Sassen 2001a). These structures

FIG. 14. FARS data from the 29 Mar 1999 cirrus cloud case study, showing from top to bottom fisheye photographs; CPL returned energy and δ value displays; plots of the hemispherical visible and infrared fluxes; T_b; MWR water vapor depth (in mm); LIRAD-derived visible optical depth τ; and infrared layer emittance ε.

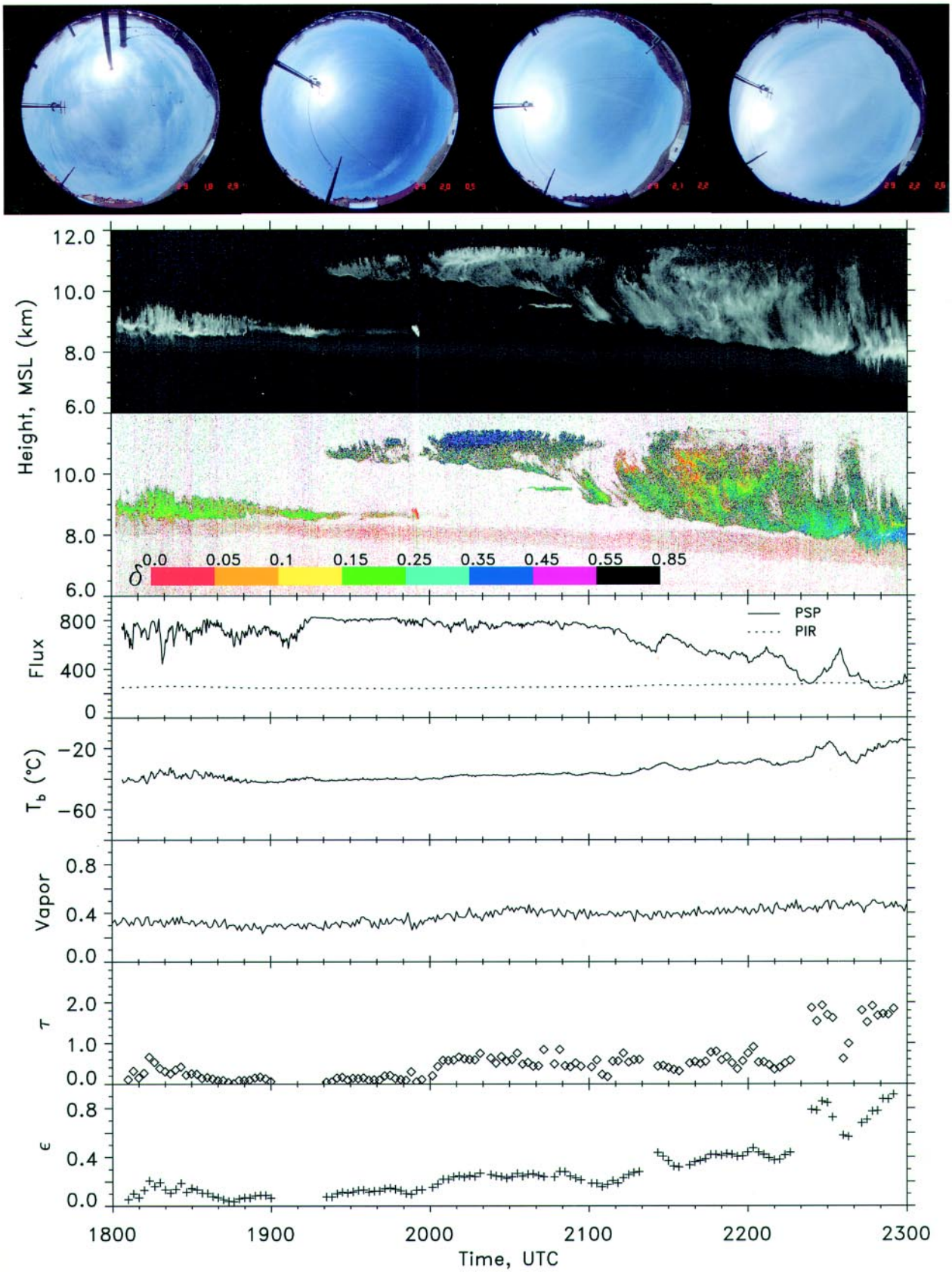
Height, MSL (km)
12.0
10.0
8.0
6.0
δ
0.0
0.05
0.1
0.15
0.25
0.35
0.45
0.55
0.85
Flux
800
400
0
PSP
PIR
T_b (°C)
−20
−60
Vapor
0.8
0.4
0.0
τ
2.0
1.0
0.0
ε
0.8
0.4
0.0
1800
1900
2000
2100
2200
2300
Time, UTC

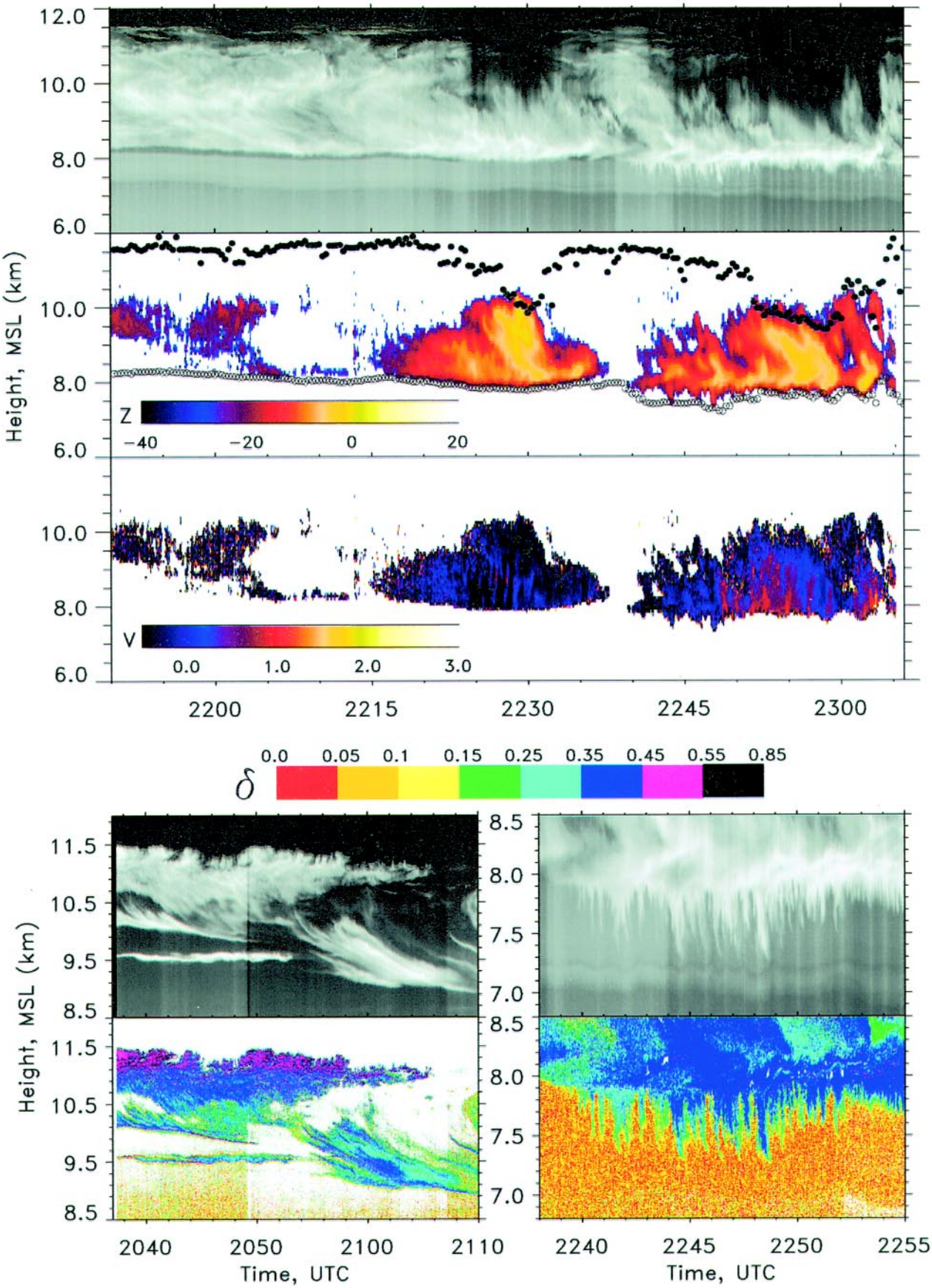
12.0
10.0
8.0
6.0
Height, MSL (km)
Z
−40
−20
0
20
V
0.0
1.0
2.0
3.0
2200
2215
2230
2245
2300
δ
0.0
0.05
0.1
0.15
0.25
0.35
0.45
0.55
0.85
11.5
10.5
9.5
8.5
8.5
8.0
7.5
7.0
2040
2050
2100
2110
2240
2245
2250
2255
Time, UTC
Time, UTC

have penetrated into dry subcloud air (Fig. 11), which also contains relatively weakly scattering aerosol. As evident in the top of Fig. 15, this sloping layer remained separated from the cirrus until the altostratus layer lowered into it. The source of this elevated aerosol can also be traced to an Asian dust storm. Reliable δ values obtained at the 0.532- and 0.694-μm wavelengths show depolarization of ~0.04–0.06, which are indicative of nonspherical dust particles somewhat smaller than the wavelengths (Mishchenko and Sassen 1998). Based on Langley plots of the morning (cloud free) MFRSR data, the combined molecular and aerosol τ ranged from 0.485 at 0.416 μm and 0.305 at 0.614 μm, to 0.145 at 0.870 μm, indicating a rather significant aerosol loading. A silver aureole was observed during the morning, and again at ~1920, due to the forward scattering from this aerosol. Such passive data can clearly complement the lidar depolarization data when collected in a coordinated fashion.

d. Precipitating mixed phase cloud system

A very different type of cloud system was studied from FARS a few months later, on 1 June 1999. This multilayered cloud system evolved from a midlevel cloud with overlying cirrus into a mixed phase nimbostratus layer that generated a trace amount of rain over the ~4 h FARS observation period. Although this case study had in situ support from a SPEC Incorporated Learjet research mission as part of our EOS satellite studies, the detailed analysis of the aircraft data will await future research.

The SLC radiosonde data in Fig. 16 reveal a deep moist layer from ~5 to 10 km, which was water saturated at ~5.5 km. Figure 17 provides fisheye photographs, CPL relative returned energy and linear depolarization, and W-band radar Z_e and V height–time displays, along with selected passive remote sensing plots. The lidar data show initially a midlevel ice cloud, followed by the brief appearance of a cirrus layer at ~10 km at ~2000, and, later, intermittent ice cloud returns at intermediate levels. The radar data show that the lidar returns were often restricted by signal dynamic range limitations and increasing optical

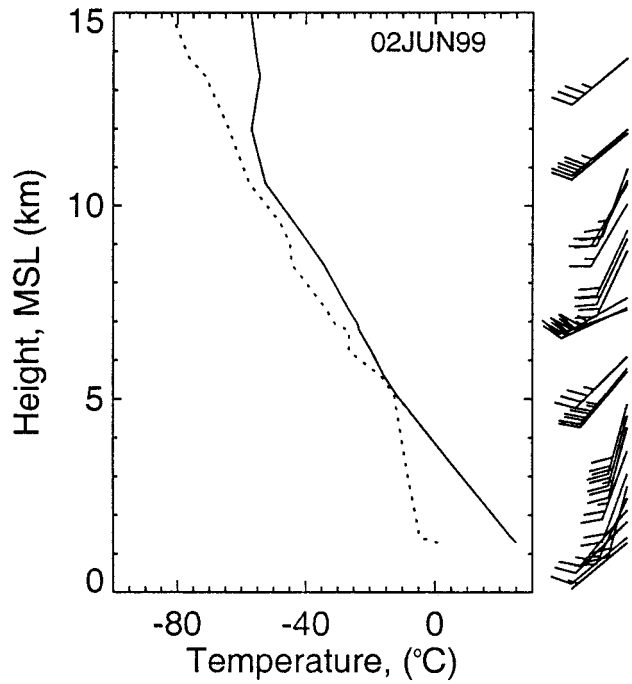

FIG. 16. SLC NWS sounding for 0000 UTC 2 Jun 1999.

extinction at midlevels, but are otherwise in reasonable agreement. Starting at ~2030, however, the range of lidar operations was severely restricted by a dense mixed phase nimbostratus cloud, such that the upper cirrus layer detected by the radar from ~8 to 10 km could no longer be sensed optically. The presence of embedded supercooled liquid water clouds is identified both by the lidar δ values, which are <0.05 at cloudbase (followed by rapid increases aloft due to the effects of multiple scattering), and the MWR liquid water depths that reach in excess of ~0.2 mm. Intercomparisons of the passive data in Fig. 17 reveal the expected inverse relation in visible and infrared radiation fluxes, and a gradual increase in MWR vapor depth accompanying the lower-level cloud development.

It can also be seen that after 2100, shafts of virga and rain became increasingly common, and at times very light rainshowers were noted at the surface. The radar V in the developing lower cloud layer show relatively small up- and downward vertical motions, except during the precipitation episodes when $V > 3$ m s^{-1} due to raindrops are evident near the surface. Although not a classic case, a slight reflectivity bright band and V increases are found at a height of 3.2 km where the snow changes to rain, particularly at ~2300.

In Fig. 18 are provided detailed views of the 0.532-μm channel PDL data, which more clearly show

FIG. 15. Additional data displays of the thickening cirrostratus studied on 29 Mar 1999 of 0.532-μm PDL returned energy, W-band equivalent radar reflectively factor in dBZ$_e$, and mean Doppler velocity V (m s^{-1}, where blue to black is upward). At bottom are shown expanded PDL displays of a mesoscale cirrus generating mass, and cirrus mammatta penetrating into dry subcloud air containing an Asian dust layer.

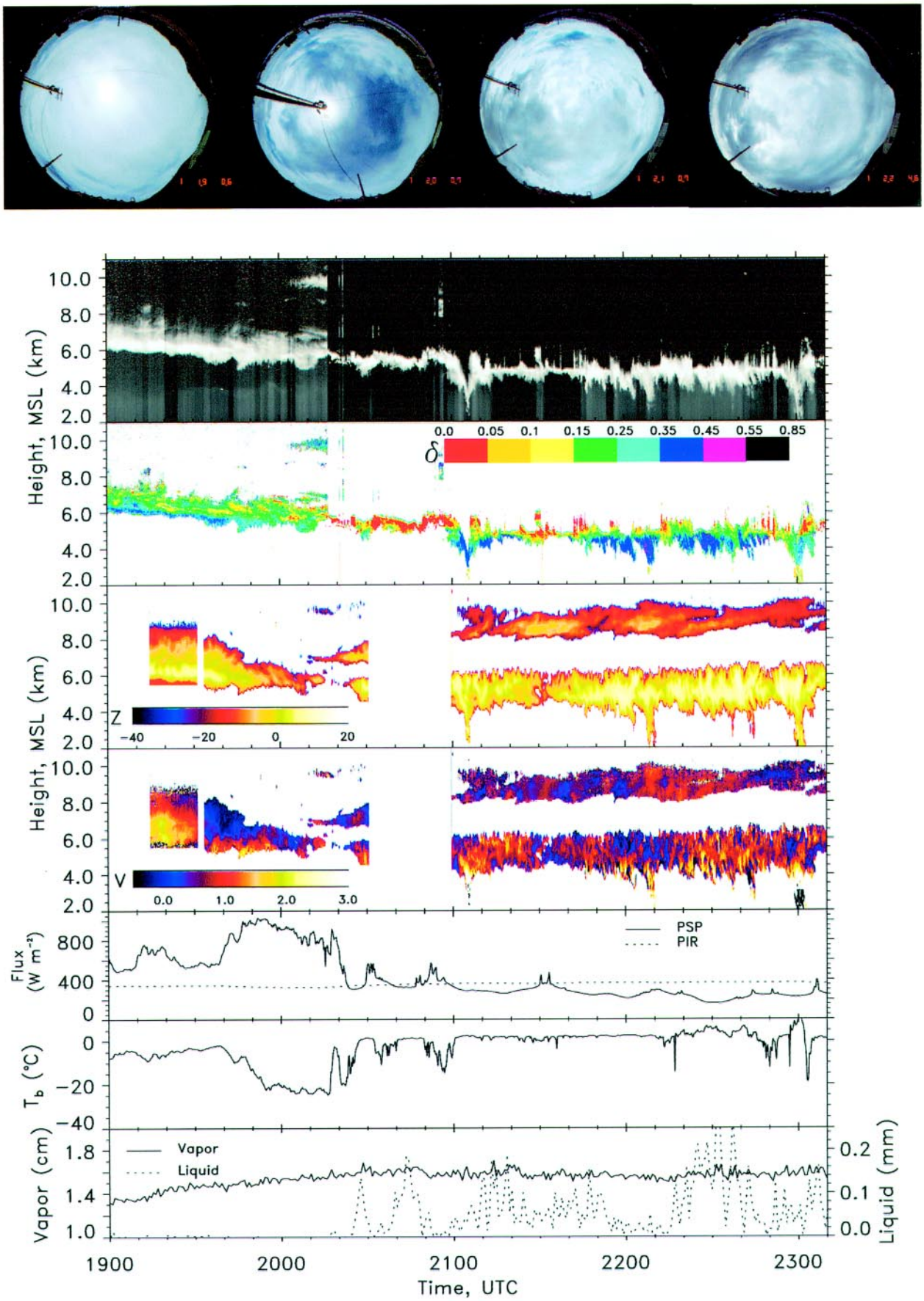
Height, MSL (km)
10.0
8.0
6.0
4.0
2.0
0.0 0.05 0.1 0.15 0.25 0.35 0.45 0.55 0.85
δ
Z
−40 −20 0 20
V
0.0 1.0 2.0 3.0
Flux (W m⁻²)
800
400
0
PSP
PIR
T_b (°C)
0
−20
−40
Vapor (cm)
1.8
1.4
1.0
Vapor
Liquid
Liquid (mm)
0.2
0.1
0.0
1900
2000
2100
2200
2300
Time, UTC

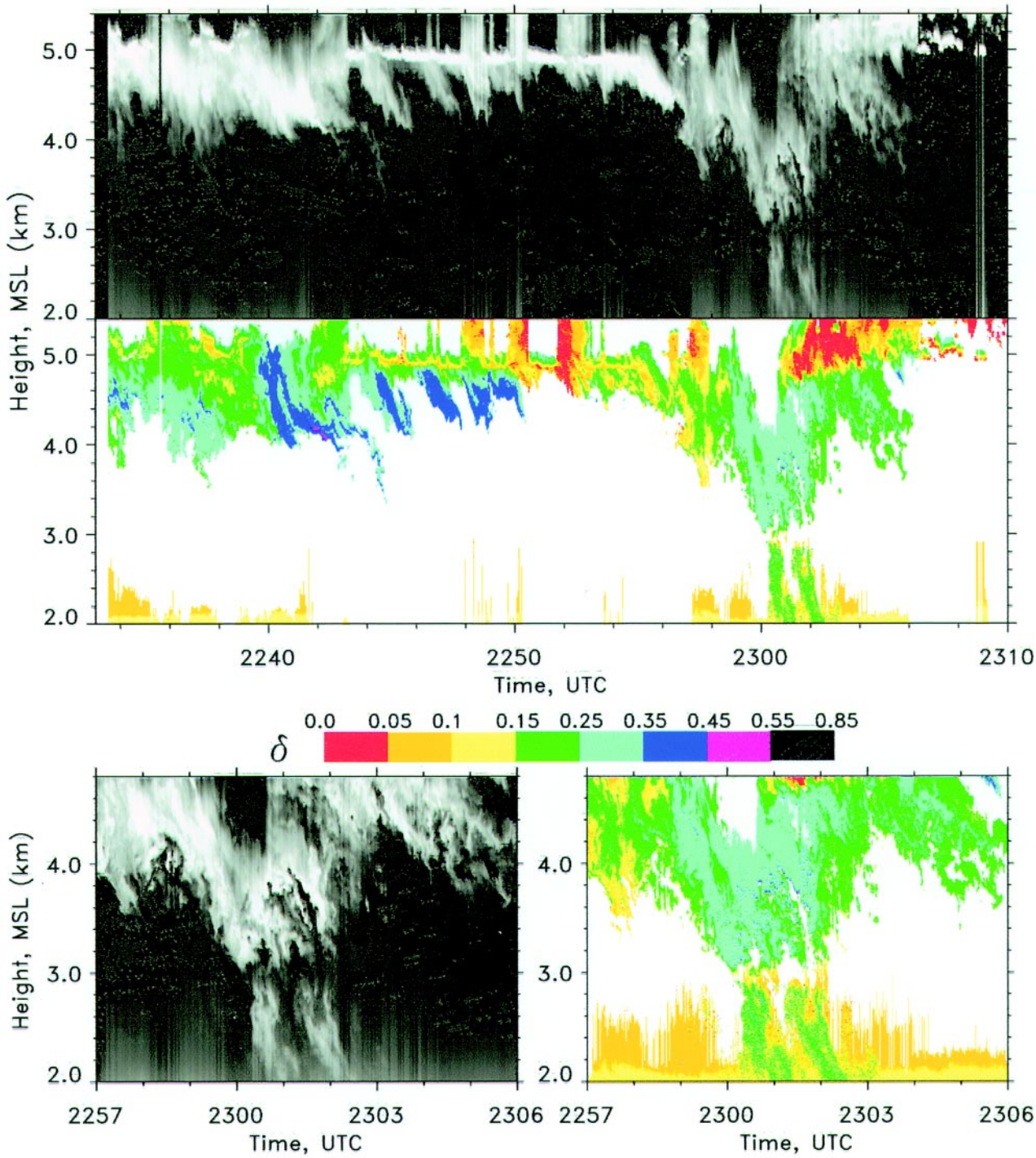

FIG. 18. Detailed views of 0.532-μm PDL backscattering and depolarization displays as precipitation developed on 1 Jun 1999. At bottom are shown expanded images of the precipitation shaft at ~2300.

FIG. 17. The FARS case study for 1 Jun 1999 following the development of a precipitating nimbostratus cloud layer. From top to bottom are shown representative fisheye photographs, time–height displays of CPL returned energy and depolarization, W-band radar dBZ_e and V, and plots of broadband fluxes, T_b, and MWR liquid water and vapor depths.

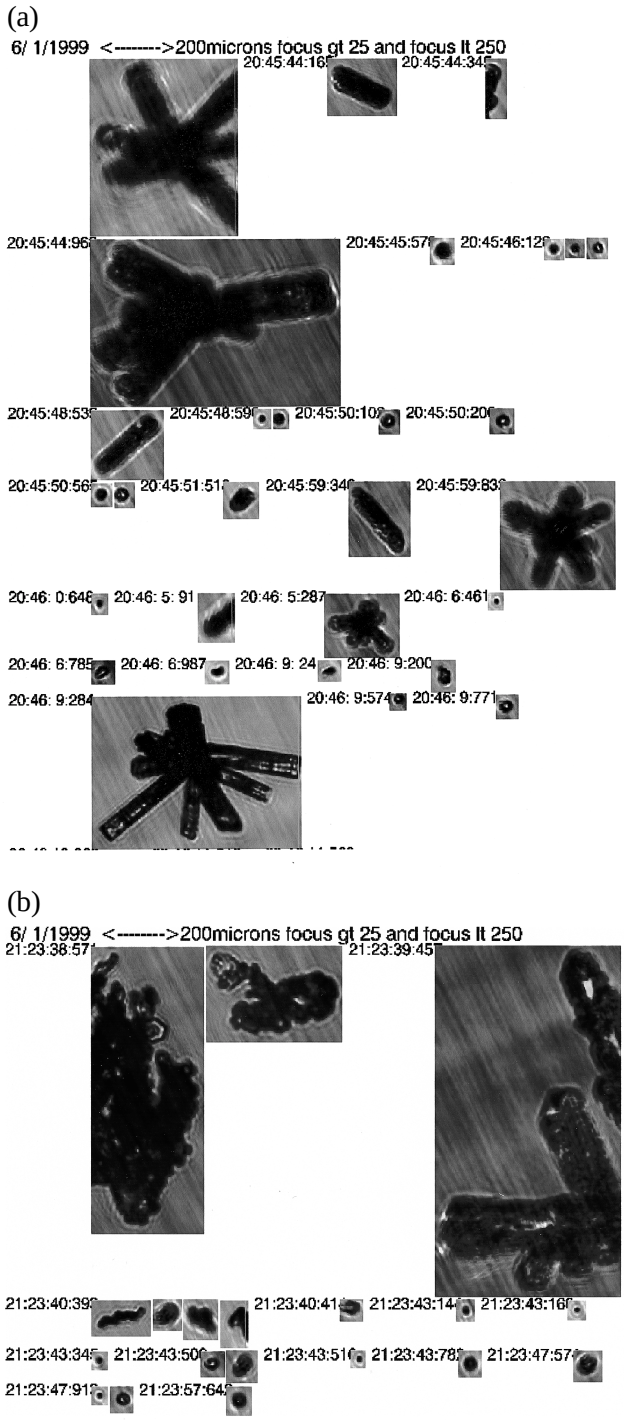

FIG. 19. Cloud Particle Imager probe data collected at the indicated times on 1 Jun 1999 showing typical (a) cirrus ice crystals (at 9.82 km and −40.4°C) and (b) particles in the lower precipitating cloud layer (at 5.33 km and −12.3°C). Note the 200-μm scales inserted at top left.

the $\delta < 0.05$ found at the liquid cloud base, followed by a rapid multiple scattering-induced depolarization increase. Although $\delta < 0.05$ are also sometimes present at about the same height due to the presence of oriented planar crystals, the SLW clouds sporadically present between 2243 and 2253 are distinguished by the strong attenuation from the numerous cloud droplets, which produce obvious range-limiting effects. The PDL returned energy and depolarization displays of the precipitation shaft at ~2300 at the bottom of Fig. 18 reveal at high (1.5 m by 0.1 s) resolution the form of the virga and precipitation. The detailed structures within the rainshafts may defy current categorization, but at a height of ~3.0 km can be seen the lidar dark band, where lidar backscattering is quite weak. Lidar depolarization in the rainshafts is up to ~0.2 which may reflect the drop shape oscillations induced by aerodynamic drag forces and turbulence effects, or large melting ice particles. Near the surface, δ values reach 0.10–0.15 in a boundary layer containing nonspherical aerosols.

Finally, given in Figs. 19a and 19b are examples of the types of ice crystals sampled in situ by the new laser-based Cloud Particle Imager probe (Lawson et al. 2001) aboard the supporting Learjet. Figure 19a shows the particles typical of the upper cirrus layer: bullet rosettes, columns, and small plate crystals. The particles in Fig. 19b from the lower precipitating cloud layer, however, represent a portion of a large stellar crystal, rimed crystals, and minute ice and perhaps water particles. The type of planar ice crystal shown in Fig. 19b is capable of horizontal alignment during fall, and could account for the low lidar δ values sometimes observed in the lower cloud.

4. Conclusions

The foregoing description reveals FARS to be a unique university-based facility for atmospheric remote sensing research, education, and the training of a new generation of professionals. This site exemplifies the synergistic application of the multiple remote sensor approach for studying aerosols, clouds, and precipitation. Its makeup approaches the variety of remote sensors that compose the core of ARM program CART central facilities, although FARS active remote sensing data collection is limited to selected case studies, but with much greater focus. This has its advantages in that each study period has comprehensive support in terms of detailed field notes and photographic records, and the real-time monitoring of data quality. Unattended observations, despite their more continuous nature, often suffer from ambiguities in the composition of the atmospheric targets being sensed (i.e.,

what constitutes aerosol versus cloud layers), and from the compromises in instrument operational modes designed to maintain sufficient dynamic range to capture *most* situations.

In the future, we hope to continue to support the satellite validation efforts connected to polar-orbiter–GOES platforms, new-generation EOS Terra/Aqua, and the planned W-band radar CloudSat and lidar Pathfinder Instruments for Cloud and Aerosol Spaceborne Observations–Climatologie Etendue des Nuages et des Aerosols (PICASSO–CENA) satellite missions. We intend to update our submissions to the NASA Langley Distributed Active Archive Center to archive the entire FARS ETO dataset, in order to increase the usefulness of the observations for satellite validation, and testing weather and climate model predictions. We anticipate that a greater emphasis will be given to aerosol research, and to characterizing in particular mixed phase and precipitating cloud systems, using the varied FARS instrumentation. We also look forward to developing the means to investigate the utility of additional lidar Stokes–circular polarization methods, Raman nitrogen and water vapor channel additions for improved scattering parameter determination and cloud/aerosol formation studies, joint lidar–radar volume scanning methods, and W-band radar Doppler spectra studies.

Acknowledgments. Recent FARS research has been funded by NSF Grant ATM-9528287, and NASA Grants NAG-1-2083 and NAG-5-6458. Major instrument development support has come from NSF Grants ATM-8914348 (CPL and radiometer) and ATM-9214581 (W-band radar), DOE Grant DEFG02ER1059 from the Atmospheric Radiation Measurement Instrument Development Program (PDL), and NASA Grant NAG-5-6458 (MWR). The Lear jet supported by EOS funding is owned by Rainbow Chaser LLC and operated by SPEC, Incorporated.

References

Barnett, J. M., 2000: Remote sensing of midlatitude cirrus radiative properties: A seven-year climatology. Ph.D. dissertation, University of Utah, 220 pp.

Benson, S., 1999: Lidar depolarization study to infer cirrus cloud microphysics, M.S. thesis, Department of Meteorology, University of Utah, 136 pp.

Campbell, J. R., 1997: A midlatitude cirrus climatology from the ten-year Facility for Atmospheric Remote Sensing high cloud dataset. M.S. thesis, Department of Meteorology, University of Utah, 112 pp.

Cox, S. K., D. S. McDougal, D. A. Randall, and R. A. Schiffer, 1987: FIRE–The First ISCCP Regional Experiment. *Bull. Amer. Meteor. Soc.,* **77,** 114–118.

Husar, R. B., and Coauthors, 2001: The Asian dust events of 1998. *J. Geophys. Res.,* in press.

Khvorostyanov, V. I., and K. Sassen, 1998: Cloud model simulation of a contrail case study: Surface cooling versus upper tropospheric warming. *Geophys. Res. Lett.* **25,** 2145–2148.

Lawson, R. P., B. A. Baker, C. G. Schmitt, and T. L. Jenson, 2001: An overview of microphysical properties of Arctic clouds observed in May and July 1998 during FIRE ACE. *J. Geophys. Res.,* in press.

Mishchenko, M. I., and K. Sassen, 1998: Depolarization of lidar returns by small ice crystals: An application to contrails. *Geophys. Res. Lett.,* **25,** 309–312.

Platt, C. M. R., J. C. Scott, and A. C. Dilley 1987: Remote sounding of high clouds. VI. Optical properties of midlatitude and tropical cirrus. *J. Atmos. Sci.,* **44,** 729–747.

——, and Coauthors, 1994: The Experimental Cloud Lidar Pilot Study (ECLIPS) for cloud-radiation research. *Bull. Amer. Meteor. Soc.,* **75,** 1635–1654.

Sassen, K., 1980: An initial application of polarization lidar for orographic cloud seeding operations. *J. Appl. Meteor.,* **19,** 298–304.

——, 1984: Deep orographic cloud structure and composition derived from comprehensive remote sensing measurements. *J. Climate Appl. Meteor.,* **23,** 568–583.

——, 1991: Corona producing cirrus cloud properties derived from polarization lidar and photographic analyses. *Appl. Opt.,* **30,** 3421–3428.

——, 1994: Advances in polarization diversity lidar for cloud remote sensing. *Proc. IEEE,* **82,** 1907–1914.

——, 1997: Contrail-cirrus and their potential for regional climate change. *Bull. Amer. Meteor. Soc.,* **78,** 1885–1903.

——, 2000: Lidar backscatter depolarization technique for cloud and aerosol research. *Light Scattering by Nonspherical Particles: Theory, Measurements, and Geophysical Applications,* M. L. Mischenko, J. W. Hovenier, and L. D. Travis, Eds., Academic Press, 393–416.

——, 2001a: Cirrus clouds: A modern perspective. *Cirrus,* D. Lynch et al., Eds., Oxford University Press, in press.

——, 2001b: Polarization lidar observations of Asian dust storm aerosols at FARS, Salt Lake City, Utah, US. Extended Abstracts, *20th Int. Laser Radar Conf.,* Vichy, France, Institut Pierre Simon Laplace, in press.

——, and J. D. Horel, 1990: Polarization lidar and synoptic analyses of an unusual volcanic aerosol cloud. *J. Atmos. Sci.,* **47,** 2881–2889.

——, and B. S. Cho, 1992: Subvisual-thin cirrus lidar dataset for satellite verification and climatological research. *J. Appl. Meteor.,* **31,** 1274–1285.

——, and T. Chen, 1995: The lidar dark band: An oddity of the radar bright band analogy. *Geophys. Res. Lett.,* **22,** 3505–3508.

——, and V. I. Khvorostyanov, 1998: Radar probing of cirrus and contrails: Insights from 2D model simulations. *Geophys. Res. Lett.,* **25,** 975–978.

——, and J. R. Campbell, 2001: A midlatitude cirrus cloud climatology from the Facility for Atmospheric Remote Sensing. Part I: Macrophysical and synoptic properties. *J. Atmos. Sci.,* **58,** 481–496.

——, and S. Benson, 2001: A midlatitude cirrus cloud climatology from the Facility for Atmospheric Remote Sensing. Part II: Microphysical properties derived from lidar depolarization. *J. Atmos. Sci.,* **58,** in press.

——, and J. M. Comstock, 2001: A midlatitude cirrus cloud climatology from the Facility for Atmospheric Remote Sensing. Part III: Radiative properties. *J. Atmos. Sci.*, **58,** in press.
——, T. Peter, B. P. Luo, and P. J. Crutzin, 1994: Volcanic Bishop's ring: Evidence for a sulfuric acid tetrahydrate particle aureole. *Appl. Opt.*, **33,** 4602–4606.
——, J. M. Comstock, and Z. Wang, 2001: Parameterization of the radiative properties of midlatitude high and middle level clouds. *Geophys. Res. Lett.*, **28,** 729–732.
Schotland, R. M., K. Sassen, and R. J. Stone, 1971: Observations by lidar of linear depolarization ratios by hydrometeors. *J. Appl. Meteor.*, **10,** 1011–1017.
Stokes, G. M., and S. E. Schwartz, 1994: The Atmospheric Radiation Measurement (ARM) program: Programmatic background and design of the Cloud and Radiation Testbed. *Bull. Amer. Meteor. Soc.*, **75,** 1201–1221.